

# Three-Dimensional Photodissociation Dynamics of Rotational State Selected Methyl Iodide

Daiqian Xie<sup>†</sup> and Hua Guo\*

Department of Chemistry and Albuquerque High Performance Computing Center, University of New Mexico, Albuquerque, New Mexico 87131

Yoshiaki Amatatsu

Faculty of Engineering and Resource Science, Akita University, Tegata Gakuen-cho, Akita 010-8502, Japan

Ronnie Kosloff

Department of Physical Chemistry and The Fritz Haber Research Center for Molecular Dynamics, The Hebrew University, Jerusalem, 91904, Israel

Received: September 13, 1999; In Final Form: November 24, 1999

We report three-dimensional quantum mechanical calculations on the photodissociation dynamics of CH<sub>3</sub>I and CD<sub>3</sub>I on new ab initio potential energy surfaces. The improved potentials are obtained in the contracted spin-orbit configuration interaction framework by using a larger basis set and more spin-free configurations. The dynamical model includes the C–I stretch, C–H<sub>3</sub> umbrella bend, and I–C–H<sub>3</sub> bend and allows the overall rotation. The wave packet is propagated in the Chebyshev order domain. The absorption spectrum, product vibrational and rotational distributions, I\* quantum yield, and state-resolved angular distributions are calculated for the parent states of  $|JMK\rangle = |000\rangle$  and  $|111\rangle$ , and compared with experiments. The new potential energy surfaces yield a much better agreement with the experimental absorption spectrum, thanks to small potential gradients in the Franck–Condon region. The calculated rovibrational distributions of the methyl fragment are also in good agreement with experimental data. It is shown that the overall rotation has significant effects on the methyl rotational and vibrational distributions as well as the I\* yield.

## I. Introduction

Methyl iodide is an important benchmark for understanding polyatomic molecular photodissociation dynamics in the gas phase. The first ( $\bar{A}$ ) absorption band near 266 nm is structureless and attributable to the C–I  $n \rightarrow \pi^*$  transition to five repulsive dissociative states, leading to two dissociation channels CH<sub>3</sub> + I(<sup>2</sup>P<sub>3/2</sub>) (the I channel) and CH<sub>3</sub> + I(<sup>2</sup>P<sub>1/2</sub>) (the I\* channel).<sup>1</sup> Among them, three are dipole allowed. The <sup>3</sup>Q<sub>1</sub> state, which correlates to the I channel, is the weakest and lowest in energy in the Franck–Condon region. The <sup>3</sup>Q<sub>0+</sub> state, which diabatically correlates to the I\* channel, is energetically lower in the Franck–Condon region than the <sup>1</sup>Q<sub>1</sub> state, which correlates to the I channel. As a result, the two diabatic potential energy surfaces (PESs) intersect and nonadiabatic transitions play an important role in the dissociation dynamics. The nonadiabaticity manifests itself both in spectroscopy and final product state distributions. An early magnetic circular dichroism (MCD) study<sup>2</sup> indicated that the parallel <sup>3</sup>Q<sub>0+</sub> state dominates at low energies, while the perpendicular <sup>1</sup>Q<sub>1</sub> state becomes more important at high energies. The transition dipole for the lower <sup>3</sup>Q<sub>1</sub> state is significantly smaller. However, a recent product velocity imaging experiment<sup>3</sup> concluded that the MCD result overestimated the contribution of the <sup>1</sup>Q<sub>1</sub> state by  $\sim 20$ -fold, and the <sup>3</sup>Q<sub>0+</sub> state carries almost all of the oscillator strength throughout the  $\bar{A}$  band except in the high-energy wing.

There have been extensive experimental investigations of this prototypical system. The literature prior to 1992 has been

reviewed by one of us.<sup>4</sup> Subsequent reviews by Johnson et al.,<sup>5</sup> and more recently by Eppink and Parker,<sup>6</sup> provided additional and updated information on this system. In short, methyl iodide dissociates directly and promptly.<sup>7</sup> The dynamics is mostly along the C–I coordinate with some participation of the C–H<sub>3</sub> coordinate.<sup>8–12</sup> The repulsive potentials along the C–I coordinate render large energy disposal into the fragment recoil. Some vibrational excitation in the methyl fragment has been found, mostly in the umbrella bending ( $\nu_2$ ) mode due to the change from a pyramidal to planar configuration. Experiments from several groups<sup>6,13–17</sup> now agree that the methyl fragment in the I\* channel is dominated by the ground vibrational state, while in the I channel the vibrational population in the umbrella mode is slightly inverted with a peak at  $\nu = 1$ . Small but significant rotational excitation in the methyl fragment has also been observed.<sup>13,17,18,19–25</sup> In the latter case, the excitation is largely about the axis perpendicular to the C<sub>3</sub> axis of the methyl fragment, while the rotation around the figure axis is conserved. Very recently, the dissociation of oriented methyl iodide has been studied with parent rotational state ( $|J_i M_i K_i\rangle$ ) selection,<sup>23–26</sup> using electrostatic hexapolar fields.<sup>27</sup> Such quantum state-to-state experiments allow direct comparison with quantum mechanical theory and yield much more information about the dissociation dynamics.<sup>28,29</sup>

Quantum mechanical studies of the dissociation dynamics of methyl iodide have relied mostly on pseudotriatomic models. Two-dimensional collinear models, which include both the C–I and C–H<sub>3</sub> coordinates, were able to reproduce most experimental observables, including the absorption spectrum and

<sup>†</sup> Visiting Professor. Permanent address: Department of Chemistry, Sichuan University, Chengdu, Sichuan, P. R. China.

product vibrational distribution.<sup>30–33</sup> Similar models have been used to address resonance Raman experiments probing the dissociation pathway.<sup>31,34–36</sup> The dynamical study of the dissociation process was put on more solid footing when high quality ab initio PESs and their couplings were reported.<sup>37–40</sup> In particular, two-,<sup>41</sup> three-,<sup>42,4</sup> and five-dimensional quantum calculations<sup>43,44</sup> have been reported using the ab initio PESs of Amatatsu et al.<sup>39</sup> In addition to the quantum calculations, classical trajectory methods have been used to study the dissociation<sup>39,40,45</sup> and the outcome agrees in general with the quantum results. Both quantum and classical results were found in reasonably good accord with experimental measurements, but several discrepancies do exist. For instance, the calculated absorption spectrum is approximately 0.4 eV blue shifted from measurement and significantly broader, presumably due to the fact the ab initio PESs are too repulsive in the Franck–Condon region. In addition, previous theoretical models are deficient in that the total angular momentum was assumed to be zero. In those calculations, spectroscopic selection rules were not enforced and the effect of the parent molecule rotational excitation on the dissociation dynamics was not examined.

This work has a two-fold purpose. First, we report new ab initio PESs for two coupled dissociative states responsible for the  $\tilde{A}$ -band absorption. These PESs were obtained using a spin-orbit configuration interaction method with a larger basis and more configurations. An important feature of the PESs yields a better agreement with the experimental absorption spectrum than the previous version.<sup>39,40</sup> Second, we treated the dynamics more rigorously by including the overall rotation of the system and taking into account the proper selection rules. In particular, the dissociation was modeled by the recently proposed Chebyshev wave packet propagation with a three-dimensional rotating pseudotriatomic Hamiltonian. The initial wave packet was prepared, with proper selection rules, from the parent molecule rotational states ( $|J_i M_i K_i\rangle = |000\rangle$  or  $|111\rangle$ ) for both  $\text{CH}_3\text{I}$  and  $\text{CD}_3\text{I}$ . The absorption spectrum,  $\text{I}^*$  yield, methyl fragment rovibrational state distributions and their wavelength dependence were calculated and compared with experimental observations. The state-resolved angular distributions of the photofragments were also calculated for oriented parent molecules. This paper is organized as follows. Section II presents the details of the theory and computational methods. The calculated results are presented and discussed in section III. A brief conclusion is presented in section IV.

## II. Theory and Computational Methods

**A. Hamiltonian.** Based on experimental knowledge of the methyl iodide dissociation, it is reasonable to approximate the system as a pseudotriatomic molecule. The three active degrees of freedom in this model are the C–I stretch, C–H<sub>3</sub> umbrella bend, and H<sub>3</sub>–C–I bend. They are approximately represented by three Jacobi coordinates  $(R, r, \chi)$ ,<sup>4</sup> where  $R$  is the distance between I and the center of mass of CH<sub>3</sub>,  $r$  is the distance between C and the center of mass of the three H atoms, and  $\chi$  is the angle between the  $r$  and  $R$  vectors. Although the dissociation follows closely the  $C_{3v}$  geometry, the H<sub>3</sub>–C–I bending motion is important in studying the rotational excitation in the methyl fragment. It is also necessary in facilitating transitions between the  $^3\text{Q}_{0+}$  and  $^1\text{Q}_1$  electronic states.<sup>41,46</sup> The two diabatic states do not interact at the  $C_{3v}$  geometry because they belong to different symmetry species ( $2A_1$  and  $3E$ ), and transitions between the two occur when the molecule distorts from the  $C_{3v}$  geometry. The rotating molecular Hamiltonian can

be written in the body-fixed (BF) frame with two coupled electronic states ( $\hbar = 1$ )

$$\hat{H} = \left[ -\frac{1}{2\mu_R} \frac{\partial^2}{\partial R^2} - \frac{1}{2\mu_r} \frac{\partial^2}{\partial r^2} + \left( \frac{1}{2\mu_R R^2} + \frac{1}{2I_{\text{CH}_3}} \right) \hat{j}^2 + \frac{1}{2\mu_R R^2} (\hat{J}^2 - 2\hat{J}_z^2 - \hat{J}_+ \hat{j}_- - \hat{J}_- \hat{j}_+) \right] \begin{pmatrix} 1 & 0 \\ 0 & 1 \end{pmatrix} + \begin{pmatrix} V_{\text{T}}(R, r, \chi) & V_{\text{TS}}(R, r, \chi) \\ V_{\text{ST}}(R, r, \chi) & V_{\text{S}}(R, r, \chi) \end{pmatrix} \quad (1)$$

where  $\mu_R$  and  $\mu_r$  are the appropriate reduced masses. The operators  $\hat{J}$  and  $\hat{J}_z$  represent the total angular momentum and its projection onto the BF  $z$  axis,  $\hat{j}$  is the rotational angular momentum operator of the CH<sub>3</sub> fragment (see below), and  $\hat{J}_{\pm}$  and  $\hat{j}_{\pm}$  are the corresponding ladder operators. The moment of inertia of the CH<sub>3</sub> fragment is defined as before<sup>4</sup>

$$I_{\text{CH}_3} = m_{\text{H}} r_{\text{e}}^2 (1 - \cos \gamma) + \frac{m_{\text{H}} m_{\text{C}}}{3m_{\text{H}} + m_{\text{C}}} r_{\text{e}}^2 (1 + 2\cos \gamma) \quad (2)$$

where  $\gamma$  is the H–C–H angle and  $r_{\text{e}}$  ( $= 2.0484a_0$ ) is the equilibrium C–H distance. Such a treatment describes only the rotation about the axis perpendicular to the  $C_3$  axis of the methyl moiety. The neglect of the parallel part is justified since little excitation in the axial rotation has been observed experimentally. The potential matrix is discussed in the next subsection.

Because of the large I–CH<sub>3</sub> reduced mass, methyl iodide can be approximately considered as a symmetric (prolate) rotor with the figure axis along the  $R$  vector. The assumption of  $K$  (the projection of the total angular momentum  $J$  on to the BF  $z$  axis) being a good quantum number is equivalent to the centrifugal sudden (CS) approximation,<sup>47</sup> which drops the terms involving  $\hat{J}_{\pm}$  in eq 1. The approximate treatment of the overall rotation is expected to be appropriate for small total angular momentum ( $J$ ). Within the CS approximation, the reduced molecular Hamiltonian for specific  $(J, K)$  values can be expressed as

$$\hat{H}^{JK} = \left[ -\frac{1}{2\mu_R} \frac{\partial^2}{\partial R^2} - \frac{1}{2\mu_r} \frac{\partial^2}{\partial r^2} + \left( \frac{1}{2\mu_R R^2} + \frac{1}{2I_{\text{CH}_3}} \right) \hat{j}^2 + \frac{J(J+1) - 2K^2}{2\mu_R R^2} \right] \begin{pmatrix} 1 & 0 \\ 0 & 1 \end{pmatrix} + \begin{pmatrix} V_{\text{T}} & V_{\text{TS}} \\ V_{\text{ST}} & V_{\text{S}} \end{pmatrix} \quad (3)$$

**B. Potential Energy Surfaces.** Previous quantum calculations<sup>4,44</sup> have indicated that the previous version of the ab initio PESs calculated by Amatatsu et al.<sup>39,40</sup> yields an absorption spectrum that is too broad and blue shifted from the experimental one. In particular, the calculated excitation energy of 5.12 eV is about 0.35 eV larger than the experimental data. The broad spectrum implies that the PESs are too repulsive in the Franck–Condon region. The discrepancies seem to be mainly due to the quality of the spin-free diagonal elements in the contracted spin-orbit configuration interaction (SOC) calculations.

To improve the quality of the ab initio PESs in the Franck–Condon region, we tried the following scheme. The diagonal elements ( $^1A_1$ ,  $^1E$ ,  $^3E$ ,  $^3A_1$ ) in the SOC matrix were recalculated by means of the spin-free CI method. The basis set was improved by changing the valence double- $\zeta$  level to the triple- $\zeta$  one, while other inputs such as the polarization functions and relativistic effective core potential were kept the same as the previous ones. The molecular orbitals were determined by an

**TABLE 1: Modified Parameters for the Diagonal Potential for Methyl Iodide (in a.u.)<sup>a</sup>**

	$P_{i0}$	$P_{i1}$	$P_{i2}$
$A_0$	0.223327	-0.070491	-0.028627
$A_1$	-0.109315	0.142368	0.004171
$A_2$	0.019901	-0.022302	0.0
$A_4$	1.718200	-0.162716	0.128111
$A_5$	-0.032418	0.031726	0.0
$A_8$	-0.072448	0.082714	-0.055950
$A_9$	-0.004848	-0.002163	0.001635
$A_{10}$	-0.009842	0.007512	0.0
$B_0$	0.142473	-0.042826	-0.012602
$B_1$	-0.119258	0.064387	0.016015
$B_2$	0.113208	-0.139262	0.0
$B_4$	0.938154	0.276679	0.028479
$B_5$	-0.057911	0.057376	0.0
$B_8$	-0.051650	-0.132750	0.097001
$B_9$	0.0	0.0	0.0
$B_{10}$	0.0	0.0	0.0
	$Q_{i0}$	$Q_{i1}$	$Q_{i2}$
$A_3^*$	0.0	-0.322354	0.096945
$A_6^*$	0.0	0.224101	-0.141370
$A_7^*$	0.0	-0.283743	0.055487
$A_{11}^*$	0.0	0.006063	-0.002086
$B_3^*$	0.0	-0.316726	0.086647
$B_6^*$	0.0	0.220449	-0.142314
$B_7^*$	0.0	-0.290132	0.000248
$B_{11}^*$	0.0	0.0	0.0

<sup>a</sup> For details of the potential energy functions see the work of Amatatsu et al.<sup>40</sup>

open-shell restricted Hartree–Fock calculation for the average  $n \rightarrow \sigma^*$  excited states by means of the MELD program.<sup>48</sup> The second-order CI calculations with the full valence ( $\sigma$ ,  $e_x$ ,  $e_y$ ,  $\sigma^*$ ) reference configurations were performed to obtain the diagonal terms using the GAMESS program.<sup>49</sup>

The contracted SOCI matrix, which is composed of the improved diagonal elements and the unchanged off-diagonal elements, was then diagonalized to obtain the adiabatic energies for each geometry. The adiabatic potential energies were then used to fit the diabatic potential functions defined in earlier work.<sup>40</sup> In the fitting, the off-diagonal functions of the potential matrix were unchanged and a new set of potential parameters of the diagonal elements was determined by a least-squares method. Table 1 lists the new potential parameters, among which  $A_0$ ,  $A_8$ ,  $A_9$ ,  $B_0$ ,  $B_8$ ,  $A_7^*$ , and  $B_7^*$  have been modified for the three diabatic states, namely  ${}^3Q_{0+}(V_T)$ ,  ${}^1Q_1(A'$  branch,  $V_S)$ ,  ${}^1Q_1(A''$  branch,  $V_{S'})$ . Other parameters are fixed at their original values. The excitation energies of the new  ${}^3Q_{0+}$  and  ${}^1Q_1$  potentials are respectively 0.30 and 0.26 eV lower than the previous PESs. The potentials of the two states along the  $R$  coordinate are plotted in Figure 1, along with those of the 1996 version.<sup>40</sup> In the dynamical calculations reported here, only the  ${}^3Q_{0+}$  and  ${}^1Q_1$  ( $A'$  branch) potentials were included and coordinates other than the three Jacobi coordinates were fixed at their equilibrium values. The  $A''$  branch of the  ${}^1Q_1$  state is ignored since it has no interaction with the two  $A'$  states included in our calculations.

**C. Photodissociation Cross-Sections and Chebyshev Propagation.** Within the dipole approximation, the photodissociation differential cross-section from an initial parent state labeled as ( $J_i M_i K_i$ ) into an exit channel labeled as ( $\hat{k} E n$ ) is<sup>50,51</sup>

$$\sigma(\hat{k} E n | J_i M_i K_i) = \frac{\pi \omega}{c \epsilon_0} |\langle \psi^{-\hat{k} E n} | \hat{\epsilon} \cdot \boldsymbol{\mu} | \Psi^{J_i M_i K_i} \rangle|^2 \quad (4)$$

where  $\boldsymbol{\mu}$  is the transition dipole moment vector connecting the

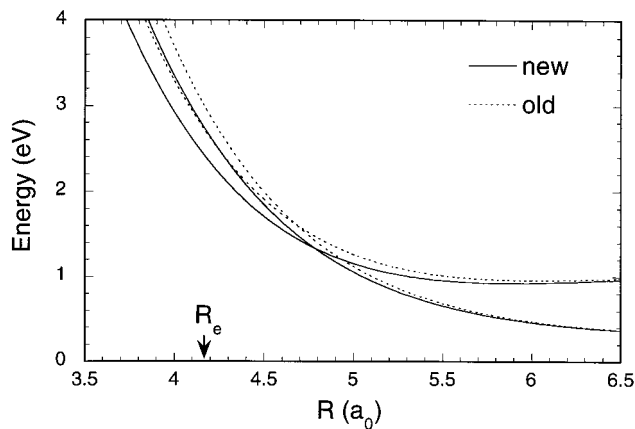


**Figure 1.** Comparison of the potentials of the two excited states with those of the 1996 version along the  $R$  coordinate.<sup>40</sup> The new potentials are energetically lower and less steep in the Franck–Condon region.

initial and final electronic states involved in the transition,  $\hat{\epsilon}$  is a unit vector in the polarization direction of the photon,  $E = \hbar \omega$  is the photon energy,  $n$  denotes collectively the quantum numbers of the final photofragments, and  $\hat{k}$  specifies the scattering angle of the fragment in space-fixed (SF) frame.  $\Psi^{J_i M_i K_i}$  represents a rovibrational wave function ( $\Psi^{J_i K_i}$ ) in the ground electronic state PES, multiplied by a symmetric rotor eigenstate ( $D_{K_i M_i}^{J_i}$ ). The cross-section in eq 4 can be calculated using either time-dependent or time-independent methods.<sup>52</sup>

In this work, we compute eq 4 using an efficient propagation method based on the Chebyshev propagator,<sup>53</sup> avoiding time propagation. The Chebyshev propagation states

$$|\Phi_k\rangle = \cos(k \arccos \hat{H}_n) |\Phi_0\rangle \quad (5)$$

can be generated recursively using the three-term Chebyshev recursion relation:<sup>54</sup>

$$|\Phi_k\rangle = 2\hat{H}_n |\Phi_{k-1}\rangle - |\Phi_{k-2}\rangle \quad (6)$$

with  $|\Phi_1\rangle = \hat{H}_n |\Phi_0\rangle$ . In the above recursion, the Hamiltonian is normalized to  $[-1, 1]$ :

$$\hat{H}_n = (\hat{H} - \bar{H}) / \Delta H \quad (7)$$

where  $\bar{H} = (H_{\max} + H_{\min})/2$  and  $\Delta H = (H_{\max} - H_{\min})/2$  are estimated from the grid used in the calculation.

The application of the Chebyshev propagation to photodissociation problems has been discussed by one of us previously.<sup>55,56</sup> The total cross-section can be calculated from a cosine Fourier transform of the autocorrelation function  $C_k^{JK, \alpha}$  ( $\equiv \langle \Phi_0^{JK, \alpha} | \Phi_k^{JK, \alpha} \rangle$ ) in the Chebyshev order domain:

$$\sigma(\theta JK | J_i M_i K_i) = \frac{2\pi \omega}{c \sin \theta} \sum_{\alpha} \sum_k \left(1 - \frac{\delta_{k0}}{2}\right) \cos(k\theta) C_k^{JK, \alpha} \quad (8)$$

where  $\theta = \arccos E$  is the Chebyshev angle<sup>57</sup> and  $\alpha = T, S$  denote the excited states involved in the initial excitation. The partial cross-section from the initial state to a specific ( $m_j$ -summed) product state is expressed as:<sup>28</sup>

$$\bar{\sigma}_\alpha(\hat{k}E\nu N|J_i M_i K_i) = \frac{4\pi^2\omega}{c} \sum_{J'K'} \sqrt{\frac{2J+1}{4\pi}} \sqrt{\frac{2J'+1}{4\pi}} D_{KM_i}^{J*}(\hat{k}) D_{KM_i}^{J'}(\hat{k}) \sum_{h' h} w(JK|h0|J_i M_i K_i) w(J'K|h'0|J_i M_i K_i) t_\alpha^*(EJK\nu N\beta|h|E_i J_i K_i) t_\alpha(E'J'K\nu N\beta|h'|E_i J_i K_i) \quad (9)$$

where  $h = K - K_i$  labels the spherical harmonics components of the transition dipole and is restricted by the selection rules,  $\nu$  and  $N$  are respectively the umbrella vibrational and rotational quantum numbers of the methyl fragment. The above expression not only gives the information on the final state distribution of the fragments but also the state-resolved angular distribution for an oriented parent molecule defined by the projection of the total angular momentum on the SF  $z'$  axis ( $M_i$ ). It thus provides a direct comparison with photodissociation experiments on oriented methyl iodide.<sup>23,24,25,26</sup>

For the majority of experiments that have no initial orientation, the scattering angle averaged partial cross-section is more appropriate:

$$\sigma_\alpha(E\nu N|J_i M_i K_i) = \frac{4\pi^2\omega}{c} \sum_{J,K} w(JK|h0|J_i M_i K_i)^2 |t_\alpha(EJK\nu N\beta|h|J_i K_i)|^2 \quad (10)$$

where  $w$  is an integral over the three Euler angles and specifies the selection rules of the transition.<sup>28,50,51</sup> The  $t$  matrix elements can be evaluated in the dissociation asymptote:<sup>56</sup>

$$t_\alpha(\theta J K \nu N \beta | h | J_i K_i) = e^{ik\theta} \left\langle \sqrt{\frac{2\pi\mu_R}{k_{\nu N}^\beta}} e^{ik_{\nu N}^\beta R} \eta_{\nu N K}(r, \chi) \left| \Phi_k^{JK, \alpha} \right. \right\rangle \quad (11)$$

The wave vectors in the I( $\beta = 1$ ) and I\*( $\beta = 2$ ) channels are given by

$$k_{\nu N}^\beta = \sqrt{2\mu_R(E - D_0 - \epsilon_{\nu N} - \epsilon_{SO}\delta_{\beta 2})} \quad (12)$$

where  $D_0$  is the dissociation energy of the I-CH<sub>3</sub> bond, which is taken as the recent experimental value of 2.41 eV.<sup>6</sup>  $\epsilon_{\nu N}$  is the rovibrational energy of CH<sub>3</sub> corresponding to the rovibrational eigenstate  $\eta_{\nu N K}(r, \chi) = P_N^{K|}(\chi)\varphi_\nu(r)$ , where  $P_N^{K|}$  is the associated Legendre function and  $\varphi_\nu$  is obtained numerically by diagonalizing the fragment Hamiltonian

$$\left[ -\frac{1}{2\mu_r} \frac{\partial^2}{\partial r^2} + V_1(R \rightarrow \infty, r, 0) - \epsilon_\nu \right] \varphi_\nu(r) = 0 \quad (13)$$

Because of the nonadiabatic coupling, a wave packet starting on any diabatic state will eventually lead to both the I and I\* channels, which are separated by the spin-orbit splitting of the iodine atom ( $\epsilon_{SO} = 0.943$  eV).

**D. Initial Wave Packet.** The ground ( $\tilde{X}$ ) state wave function  $\Psi^{J_i K_i}$  used in the calculation corresponds to the lowest vibrational state with total angular momenta quantum numbers  $J_i K_i$ . It is determined using the Lanczos algorithm,<sup>58</sup> which converges very rapidly. The ground state PES is obtained from a two-dimensional ( $R, r$ ) empirical potential<sup>31</sup> in which the equilibrium geometry is replaced by the ab initio values, plus a harmonic bending potential with a force constant consistent with the experimental frequency. Table 2 shows that the calculated

**TABLE 2: Fundamental Frequencies (cm<sup>-1</sup>) for CH<sub>3</sub>I( $\tilde{X}$ ) and CD<sub>3</sub>I( $\tilde{X}$ )**

mode	CH <sub>3</sub> I theory	CH <sub>3</sub> I exp <sup>59</sup>	CD <sub>3</sub> I theory	CD <sub>3</sub> I exp
$\nu_3$	524	528	490	502
$\nu_6$	881	883	651	675
$\nu_2$	1244	1254	949	975

vibrational fundamental frequencies for both CH<sub>3</sub>I and its deuterated isotope are in reasonably good agreement with experiment.<sup>59</sup>

The selection rules for the electronic excitation are governed by the  $w$  factor in eq 9. For the parallel transition to the <sup>3</sup>Q<sub>0+</sub> state,  $J = J_i$  (forbidden if  $K=0$ ),  $J_i \pm 1$ , and  $K = K_i$ . For the perpendicular transition to the <sup>1</sup>Q<sub>1</sub> state, on the other hand,  $J = J_i$ ,  $J_i \pm 1$ ,  $K = K_i \pm 1$ .<sup>60</sup> The projection of  $J$  on the SF  $z'$  axis ( $M_i$ ) is always conserved. For the parent state of  $|J_i K_i\rangle = |00\rangle$ , the nonvanishing initial wave packets ( $\Phi_0^{JK, \alpha}$ ) on the excited state are

$$\text{parallel } (^3Q_{0+}): \Phi_0^{10, T} = \mu_0 \Psi^{00}$$

$$\text{perpendicular } (^1Q_1): \Phi_0^{11, S} = \mu_1 \Psi^{00} \quad \Phi_0^{-1, S} = \mu_{-1} \Psi^{00}$$

where  $\mu_h$  ( $h = -1, 0, 1$ ) are the spherical components of the transition dipole moments obtained from the ab initio calculation:<sup>40</sup>  $\mu_0 = 0.1531$ , and  $\mu_{\pm 1} = \mp 0.03401 - i0.03401$ .

For the parent state of  $|J_i K_i\rangle = |11\rangle$ , the nonvanishing initial wave packets are

$$\text{parallel } (^3Q_{0+}): \Phi_0^{11, T} = \mu_0 \Psi^{11} \quad \Phi_0^{21, T} = \mu_0 \Psi^{11}$$

$$\text{perpendicular } (^1Q_1): \Phi_0^{10, S} = \mu_{-1} \Psi^{11} \quad \Phi_0^{20, S} = \mu_{-1} \Psi^{11} \\ \Phi_0^{22, S} = \mu_1 \Psi^{11}$$

Since the above initial states do not couple with each other, individual propagations can be carried out for different  $JK$  values and the final outcome is summed over all the propagations weighted by the transition dipoles.

### III. Results

The two nuclear wave packets were discretized using an  $n_R \times n_r \times n_\chi$  direct-product discrete variable representation (DVR) grid. In our calculations, 512 equidistant sine DVR<sup>61</sup> points in the  $R$  coordinate were used spanning the range of  $[3.5, 17]a_0$ , 40 Gauss-associated Legendre quadrature grid<sup>62,63</sup> points were employed to represent the angular coordinate, and the  $r$  coordinate was represented by a 20 point potential optimized DVR<sup>64</sup> grid determined from eq 13 with 50 equidistant sine DVR points over the range of  $[-1.6, 1.6]a_0$ . Fast Fourier transform (FFT)<sup>65</sup> was used for the evaluation of the kinetic energy operator in the  $R$  coordinate. The wave packet was propagated with 1200 Chebyshev steps, when the center of the final wave packet is located approximately  $16a_0$ .

**A. Absorption Spectra.** The absorption spectrum was calculated from the cosine Fourier transform of the Chebyshev autocorrelation function with  $k = 300$ . The autocorrelation function decays to less than  $10^{-5}$  within approximately  $k = 100$  and never recurs, as the wave packet moves rapidly out of the Franck-Condon region. The calculated absorption spectra for both CH<sub>3</sub>I and CD<sub>3</sub>I from the nonrotating vibrational ground state ( $|J_i M_i K_i\rangle = |000\rangle$ ) are given in Figure 2. Our results show that the parallel absorption spectrum of CH<sub>3</sub>I peaks at 39980 cm<sup>-1</sup> with a half width of 4845 cm<sup>-1</sup>, while the perpendicular one peaks at 42370 cm<sup>-1</sup> with a half width of 5805 cm<sup>-1</sup>. The

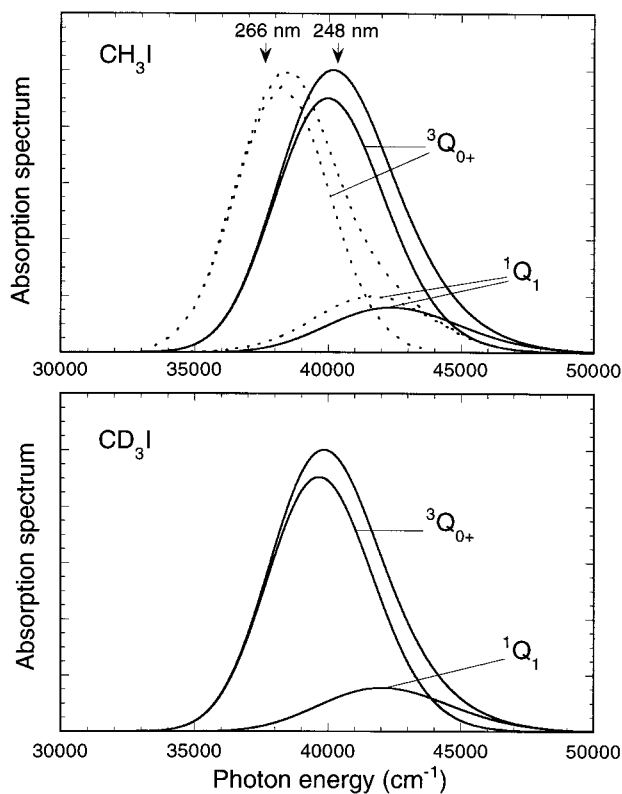


**Figure 2.** Absorption spectra of CH<sub>3</sub>I and CD<sub>3</sub>I. The dotted lines are the experimental MCD decomposition of the CH<sub>3</sub>I spectrum,<sup>2</sup> while the solid lines are obtained theoretically on the new potentials.

total spectrum peaks at 40170 cm<sup>-1</sup> with a half width of 5205 cm<sup>-1</sup>.

The MCD decomposed spectrum of CH<sub>3</sub>I,<sup>2</sup> also shown in the same figure in dotted lines, has a parallel component with a maximum at 38300 cm<sup>-1</sup> and a half width of 4120 cm<sup>-1</sup>, and a perpendicular one at 41700 cm<sup>-1</sup> with a half width of 5120 cm<sup>-1</sup>. The total absorption spectrum peaks at 38420 cm<sup>-1</sup> with a half width of 4600 cm<sup>-1</sup>. The calculated parallel absorption component has a blue shift of 1680 cm<sup>-1</sup> from the MCD data and is broader than the corresponding experimental spectrum by 725 cm<sup>-1</sup>. Similar differences also exist for the perpendicular component.

The absorption spectra reported here represent a significant improvement over those calculated with the previous version of the CH<sub>3</sub>I PESs.<sup>39,40</sup> First, the new spectra are considerably narrower, in better agreement with experiment. Second,  $D_0$  used in this work (2.41 eV), adopted from the latest experiment,<sup>6</sup> is about 0.14 eV larger than the one used in previous calculations.<sup>4</sup> In other words, the blue shift of the absorption on the previous PESs would have been ~4400 cm<sup>-1</sup> if the same  $D_0$  were used. The improvements are a direct result of the better quality of the PESs in the Franck–Condon region.

The remaining discrepancies in the absorption spectrum may be due to a number of reasons. The neglect of some degrees of freedom may be responsible. It is also conceivable that the ab initio PESs may still overestimate the C–I repulsion in the Franck–Condon region, a common feature found in other systems.<sup>66</sup> Another possible problem may come from the calculated transition dipole moments. As seen in Figure 2, the <sup>1</sup>Q<sub>1</sub> state carries approximately a quarter of oscillator strength according to the ab initio dipole moments. While in reasonable agreement with the MCD decomposition, this result is at odds with the recent product anisotropy-based decomposition, which indicated that the contribution from the <sup>1</sup>Q<sub>1</sub> state is negligible,

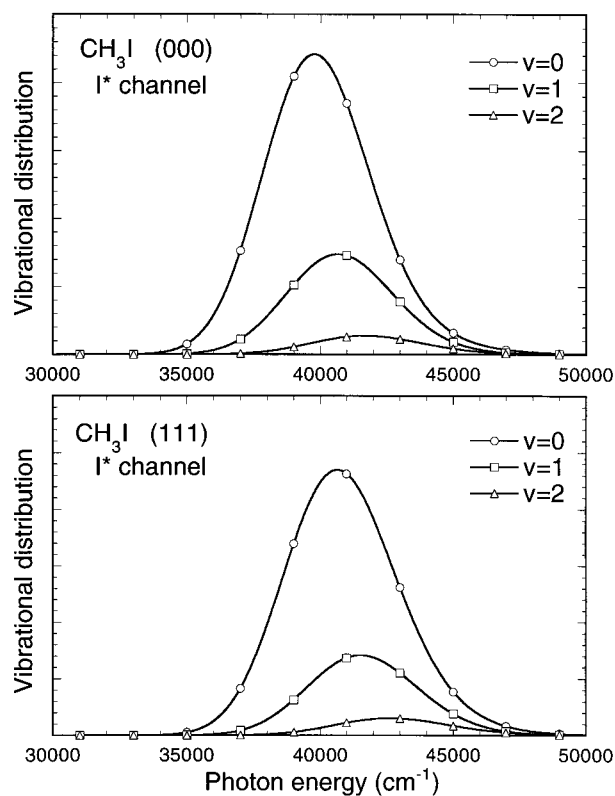


**Figure 3.** Calculated vibrational distributions of CH<sub>3</sub> in the I\* channel from the |000> (upper panel) and |111> (lower panel) states. Both the parallel and perpendicular transitions are included.

except in the high-energy wing of the  $\tilde{A}$  band.<sup>3</sup> If the latter conclusion is indeed valid, the total absorption is almost exclusively that of the <sup>3</sup>Q<sub>0+</sub> state near the peak of the spectrum. In that case, the agreement is better: 38420/39980 cm<sup>-1</sup> for the peak position and 4600/4845 cm<sup>-1</sup> for the half width.

The absorption spectra of CD<sub>3</sub>I have very similar behaviors to those of CH<sub>3</sub>I. The dominant parallel spectrum peaks at 39670 cm<sup>-1</sup> with a half width of 4650 cm<sup>-1</sup>, while the perpendicular spectrum maximizes at 42030 cm<sup>-1</sup> with a half width of 5475 cm<sup>-1</sup>. The results indicate that the total absorption spectrum of CD<sub>3</sub>I is about 300 cm<sup>-1</sup> red shifted relative to the CH<sub>3</sub>I spectrum and has a width about 200 cm<sup>-1</sup> narrower.

**B. Vibrational Distributions.** The umbrella vibrational distributions of the methyl fragment are more sensitive to the global properties of the PESs than the absorption spectra and thus provide more detailed information about the photodissociation dynamics and the quality of the ab initio PESs. In our calculations, 1100 Chebyshev propagation steps were carried out before the wave packets were projected to the asymptotic basis. Projections at larger  $k$  confirmed the convergence in the product rotational and vibrational distributions. The total cross-section obtained from summing over all the fragment rotational and vibrational distributions agrees very well with that from the Fourier transform of the autocorrelation function, further confirming the self-consistency of the calculation. The vibrational distributions of the methyl fragment were obtained by summing over all the rotational states related to the given vibrational states.

Figure 3 shows the CH<sub>3</sub> umbrella vibrational distribution in the dominant I\* channel as a function of the photon energy. The upper and lower panels display vibrational distributions from the initial parent states of  $|J_i M_i K_i\rangle = |000\rangle$  and  $|111\rangle$ , with proper selection rules discussed in IID. The two distributions show similar behaviors. For example, there is no population

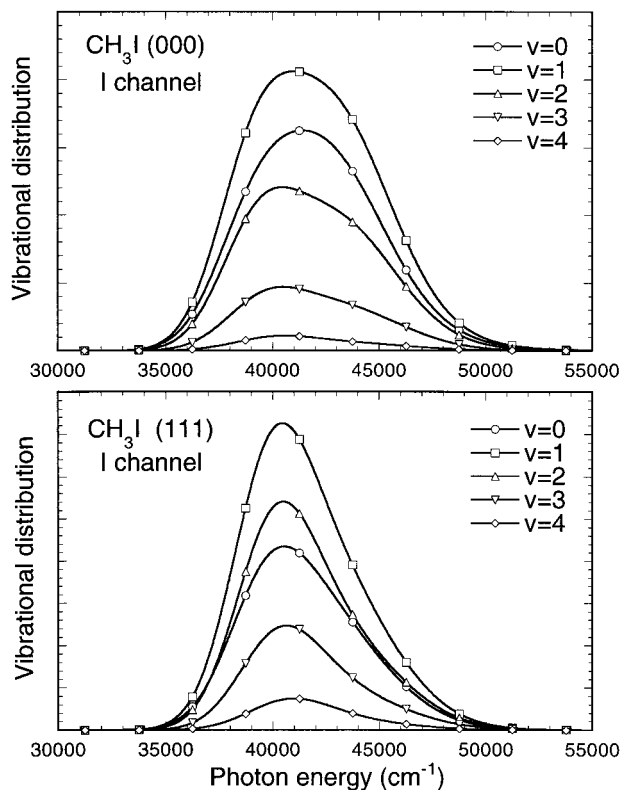


**Figure 4.** Calculated vibrational distributions of CH<sub>3</sub> in the I channel from the |000> (upper panel) and |111> (lower panel) states. Both the parallel and perpendicular transitions are included.

inversion and the ratio of  $\nu = 0/\nu = 1$  at the 266 nm is 5.60 and 8.00, respectively. For the initial state of  $|J_i M_i K_i\rangle = |000\rangle$ , the calculated ratio is in excellent agreement with the most recent experimental ratio of 5.06.<sup>3</sup> The |111> initial state, however, produces a slightly colder distribution. Overall, the influence of the parent rotation is minor in this channel.

Figure 4 displays the corresponding CH<sub>3</sub> vibrational distributions in the I channel. It shows that the distribution is inverted with a peak at  $\nu = 1$  in both cases. However, the quantitative distributions depends on the overall rotation of CH<sub>3</sub>I. The |111> parent state yields a hotter distribution than the |000> state, in contrast to the case of the I\* channel.

The difference in vibrational excitation in the two dissociation channels can be traced back to the topology of the PESs involved in the dissociation.<sup>32,39,40</sup> The <sup>3</sup>Q<sub>0+</sub> PES has its *r* equilibrium very close to the ground state geometry in the Franck–Condon region, and the pyramidal CH<sub>3</sub> is switched smoothly to the planar geometry as CH<sub>3</sub>I dissociates. Thus, the C–H<sub>3</sub> coordinate experiences little force and the final vibrational excitation is minimal. On the other hand, the equilibrium geometry in the *r* coordinate of the <sup>1</sup>Q<sub>1</sub> PES is quite different from that of the  $\tilde{X}$  state. Thus, dissociation on the <sup>1</sup>Q<sub>1</sub> PES produces more vibrational excitation.

To better understand the influence of the initial excitation, we present in Figure 5 the CH<sub>3</sub> vibrational state distributions in both the I and I\* channels with the exclusively parallel excitation of the  $|J_i M_i K_i\rangle = |000\rangle$  state. In the I\* channel, the distribution is similar to the upper panel in Figure 3 since the influence of the perpendicular excitation in this channel is minimal. As expected, the perpendicular excitation has a more pronounced effect on the vibrational distribution in the I channel, due to its correlation to the <sup>1</sup>Q<sub>1</sub> state. This can be readily seen by comparing the lower panel of Figure 5 with the upper panel in Figure 4. While the  $\nu = 1$  state has the highest population in

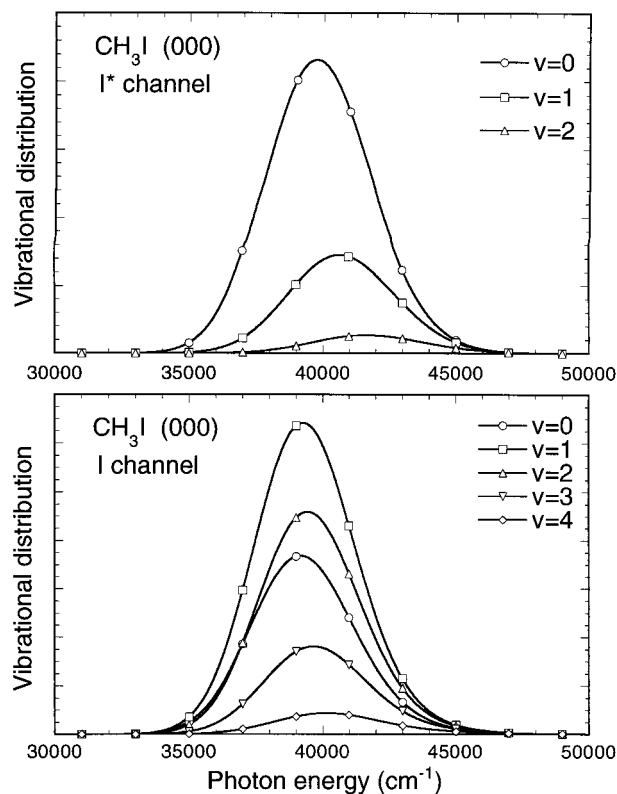


**Figure 5.** Calculated vibrational distributions of CH<sub>3</sub> in the I\* (upper panel) and I (lower panel) channels from the |000> state. Only the parallel transition is included.

both cases, the  $\nu = 0$  state is more populated than  $\nu = 2$  in Figure 4, but the reverse is true in Figure 5. Also noted is the energy dependence of the distributions. The parallel/perpendicular mixed distributions show much stronger dependence on *E*, which can be attributed to the combination effect of different dissociation pathways facilitated by nonadiabatic transitions. As a hypothetical experiment, we also calculated vibrational distributions for dissociation with *J* = 0. The difference in the I\* channel is minimal, while some quantitative changes were found in the I channel.

To compare our calculated results with experiments and previous theoretical calculations, we list in Tables 3 and 4 CH<sub>3</sub> vibrational distributions in both dissociation channels at two photon wavelengths. At 248 nm, our results are in excellent agreement with the experimental data of Zhu et al.<sup>16</sup> in both the I\* and I channels and those of Suzuki et al. in the I\* channel.<sup>15</sup> The agreement is much better than previous 3D<sup>4</sup> and 5D quantum mechanical (QM) calculations,<sup>44</sup> and consistent with the broad band classical trajectory (CT) calculations of Amatatsu et al.,<sup>39</sup> all of which used the previous version of PESs. At 266 nm, the vibrational distribution is colder than at 248 nm. The agreement with the experimental data of Eppink and Parker<sup>6</sup> is fairly good, although our calculations seem to yield a colder distribution in both dissociation channels. Overall, the agreement is quite satisfactory. The discrepancy in the absorption spectra should not change the picture qualitatively since the vibrational distributions are not strongly wavelength dependent.

Figure 6 presents the CD<sub>3</sub> vibrational distributions in both the I\* and I channels from the photodissociation of CD<sub>3</sub>I prepared in the  $|J_i M_i K_i\rangle = |000\rangle$  and |111> states. Both parallel and perpendicular transitions are included. In the I\* channel, the population decreases monotonically with the umbrella vibrational quantum number, similar to the CH<sub>3</sub>I case. This is

**TABLE 3: Vibrational Distribution of CH<sub>3</sub> from the 248 nm Photodissociation of CH<sub>3</sub>I (000)**

	exp <sup>15</sup>	exp <sup>16</sup>	CT <sup>39,40a</sup>	3D QM <sup>4</sup>	5D QM <sup>44</sup>	this work (mixed)	this work (pure <sup>3</sup> Q <sub>0+</sub> )
I*, $\nu = 0$	0.65	0.66	0.74	0.53	0.79	0.72	0.71
I*, $\nu = 1$	0.28	0.26	0.19	0.38	0.20	0.24	0.25
I*, $\nu = 2$	0.06	0.08	0.06	0.09	0.01	0.04	0.04
I, $\nu = 0$	0.23		0.14	0.13	0.27	0.29	0.21
I, $\nu = 1$	0.33		0.32	0.35	0.56	0.38	0.37
I, $\nu = 2$	0.23		0.37	0.32	0.16	0.22	0.28
I, $\nu = 3$	0.12		0.11	0.15	0.01	0.09	0.11
I, $\nu = 4$	0.04		0.04	0.05		0.02	0.03

<sup>a</sup> Classical trajectory results are for broad band excitation.

**TABLE 4: Vibrational Distribution of CH<sub>3</sub> from the 266 nm Photodissociation of CH<sub>3</sub>I (000)**

	exp <sup>6</sup>	CT <sup>45</sup>	3D QM <sup>4</sup>	5D QM <sup>44</sup>	this work (mixed)	this work (pure <sup>3</sup> Q <sub>0+</sub> )
I*, $\nu = 0$	0.63	0.47	0.58	0.76	0.84	0.84
I*, $\nu = 1$	0.28	0.26	0.36	0.22	0.15	0.15
I*, $\nu = 2$	0.07	0.14	0.06	0.02	0.01	0.01
I, $\nu = 0$	0.19	0.19	0.16	0.32	0.28	0.24
I, $\nu = 1$	0.27	0.27	0.39	0.54	0.39	0.39
I, $\nu = 2$	0.22	0.20	0.30	0.13	0.23	0.26
I, $\nu = 3$		0.17	0.11	0.01	0.08	0.09
I, $\nu = 4$		0.05	0.03		0.01	0.02

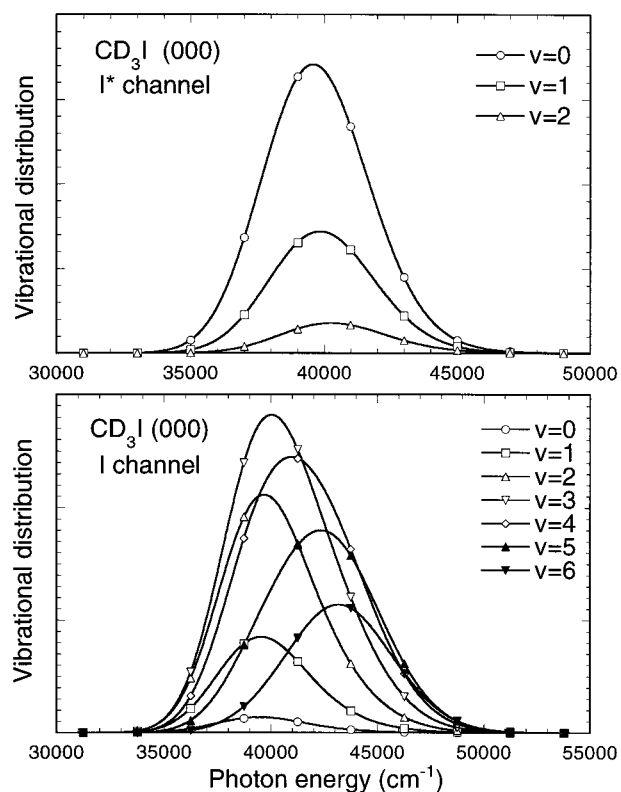
**TABLE 5. Calculated Vibrational Distribution of CD<sub>3</sub> from the Photodissociation of CD<sub>3</sub>I (000)**

	266 nm (mixed)	266 nm (pure <sup>3</sup> Q <sub>0+</sub> )	248 nm (mixed)	248 nm (pure <sup>3</sup> Q <sub>0+</sub> )
I*, $\nu = 0$	0.70	0.70	0.64	0.63
I*, $\nu = 1$	0.25	0.25	0.28	0.28
I*, $\nu = 2$	0.05	0.05	0.07	0.07
I, $\nu = 0$	0.02	0.02	0.01	0.02
I, $\nu = 1$	0.11	0.11	0.08	0.11
I, $\nu = 2$	0.26	0.27	0.20	0.27
I, $\nu = 3$	0.31	0.32	0.27	0.32
I, $\nu = 4$	0.20	0.20	0.23	0.20
I, $\nu = 5$	0.08	0.07	0.13	0.07
I, $\nu = 6$	0.02	0.01	0.06	0.01

consistent with earlier quantum<sup>44</sup> and classical calculations.<sup>40</sup> The calculated population ratio for the three lowest states is 1.0:0.44:0.11 at 248 nm. This can be compared with the IR absorption experimental ratio of 1.0:0.75:0.5 (~20% uncertainty)<sup>14</sup> and TOF experimental data of 0.93:1.0:0.5.<sup>16</sup> (Note the uncertainty and inconsistency of the experimental data.) Apparently, the agreement is not as good as in the CH<sub>3</sub>I case, but not unacceptable. The excitation in the CD<sub>3</sub> vibration in the I channel is more pronounced than CH<sub>3</sub>. At 248 nm, for example,  $\nu = 3$  is the highest populated state for CD<sub>3</sub> whereas the CH<sub>3</sub> distribution maximizes at  $\nu = 1$ . Unfortunately, no experimental data has so far been reported for this channel. The quantum results are consistent with earlier classical trajectory results, which showed a broad band peak at  $\nu = 3$ .<sup>40</sup>

Figure 7 displays CD<sub>3</sub> vibrational distributions in both dissociation channels with pure parallel excitation. In the I\* channel, the difference between Figures 6 and 7 is minor. In the I channel, however, the distribution with the pure parallel excitation depends weakly on the excitation frequency while that with mixed excitation shows strong frequency dependence, particularly at high frequencies where the influence of the <sup>1</sup>Q<sub>1</sub> state is large. The difference can be attributed to various nonadiabatic pathways, as discussed in the CH<sub>3</sub>I case.

**C. Rotational Distributions.** The rotation of the methyl fragment is approximately treated in our model, which can only provide information about rotation around the axis perpendicular to the C<sub>3</sub> axis of the methyl radical. Furthermore, it is incapable

**Figure 6.** Calculated vibrational distributions of CD<sub>3</sub> in the I\* (upper panel) and I (lower panel) channels from the |000> state. Both the parallel and perpendicular transitions are included.

of distinguishing the ortho and para methyl fragments. As a result, we will compare our calculated results to experimental *N* distribution with *K* = 0 or 1 for CH<sub>3</sub>/CD<sub>3</sub>. Fortunately, experimental evidence indicated that the rotational excitation in the methyl fragment is dominated by small *K*.

Our results indicate that the rotational and vibrational degrees of freedom of the methyl moiety are largely decoupled. The rotational distributions also depend weakly on the photon frequency. Figure 8 displays the vibrational state averaged CH<sub>3</sub> rotational distributions at 266 nm for two initial parent states and that from a hypothetical dissociation with *J* = 0. The inclusion of the latter case is to examine the validity of previous quantum calculations in which the total rotation was ignored.<sup>42,44</sup> These distributions indicate that the extent of the rotational excitation is slightly different in the two dissociation channels. For the |000> initial state, the I\* channel is dominated by the rotational states *N* = 1 – 6 with a peak at *N* = 2, and the I channel by the rotational states *N* = 1 – 9 with a peak at *N* = 3. Experimentally, Chandler et al.<sup>20</sup> found that at 266 nm the most dominant feature in the CH<sub>3</sub> rotational distribution (I\* channel) is *N* = 2, *K* = 0. Our distributions are also consistent with other experiments.<sup>13,17</sup> The difference in rotational excita-

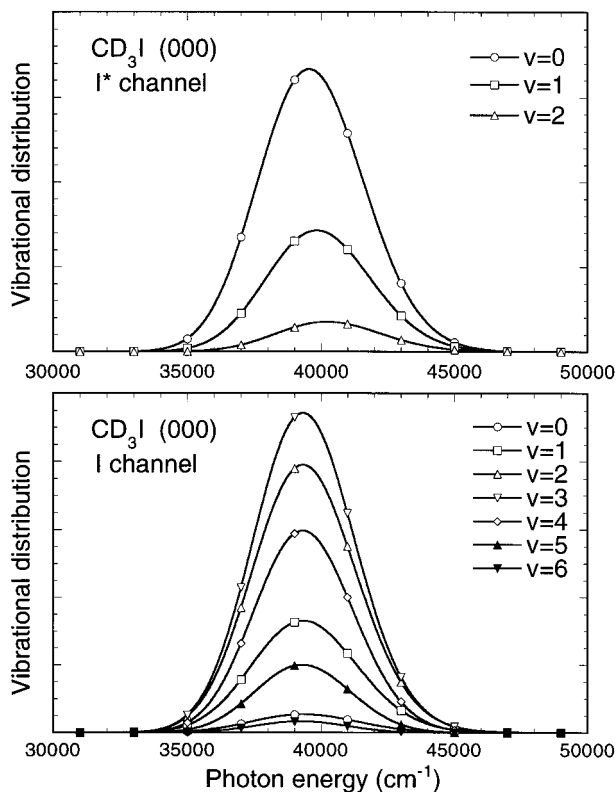


**Figure 7.** Calculated vibrational distributions of  $\text{CD}_3$  in the  $\text{I}^*$  (upper panel) and  $\text{I}$  (lower panel) channels from the  $|000\rangle$  state. Only the parallel transition is included.

tion in the two dissociation channels can be attributed to the angular anisotropy of the PESs: the angular minimum of the  ${}^1\text{Q}_1$  state is away from the  $\text{C}_{3v}$  geometry where the  ${}^3\text{Q}_{0+}$  state has its minimum at the  $\text{C}_{3v}$  geometry.<sup>39,40</sup> Consequently, the wave packet on the  ${}^1\text{Q}_1$  state experiences a larger torque, which leads to more rotational excitation.

The  $\text{CH}_3$  rotational distribution is to a limited extent affected by the overall rotation of the parent molecule. The  $\text{I}$  channel distribution obtained with the artificial constraint of  $J = 0$  (lower panel in Figure 8) differs slightly from the one with a nonzero ( $J = 1$ ) angular momentum (upper panel in Figure 8) excited from  $|J_i M_i K_i\rangle = |000\rangle$ . The difference can be attributed to the perpendicular excitation which changes the  $J, K$  value by 1 and results in a slightly hotter rotational distribution. Because the transition dipole to the  ${}^1\text{Q}_1$  state is much smaller than that to the  ${}^3\text{Q}_{0+}$  state, however, the total rotational distribution is obviously dominated by the  $K = 0$  component. The dissociation of the  $|J_i M_i K_i\rangle = |111\rangle$  state (middle panel in Figure 8) yields much more rotational excitation due to its larger  $J$  and  $K$ , as specified by the selection rules outlined in section IID. These examples underscore the importance of the parent rotation in the photodissociation. We have also carried out calculations with pure parallel excitation, and the distributions are qualitative similar to those shown in Figure 8.

Vibrational state averaged rotational distributions of  $\text{CD}_3$  are given in Figure 9. Excitation to higher rotational states is found for  $\text{CD}_3$ . Like the  $\text{CH}_3$  case, the  $\text{I}$  channel has a slightly higher degree of rotational excitation than the  $\text{I}^*$  channel. The dependence on the parent rotation is also similar to the  $\text{CH}_3$  case. The rotational distributions from the  $|111\rangle$  parent state are particularly interesting because several recent experiments have studied the  $\text{CD}_3$  rotational distribution upon the dissociation of oriented parent states at 266 nm.<sup>23–25</sup> The latest experiment of Janssen et al.,<sup>25</sup> for example, found that the  $\text{CD}_3$  rotational

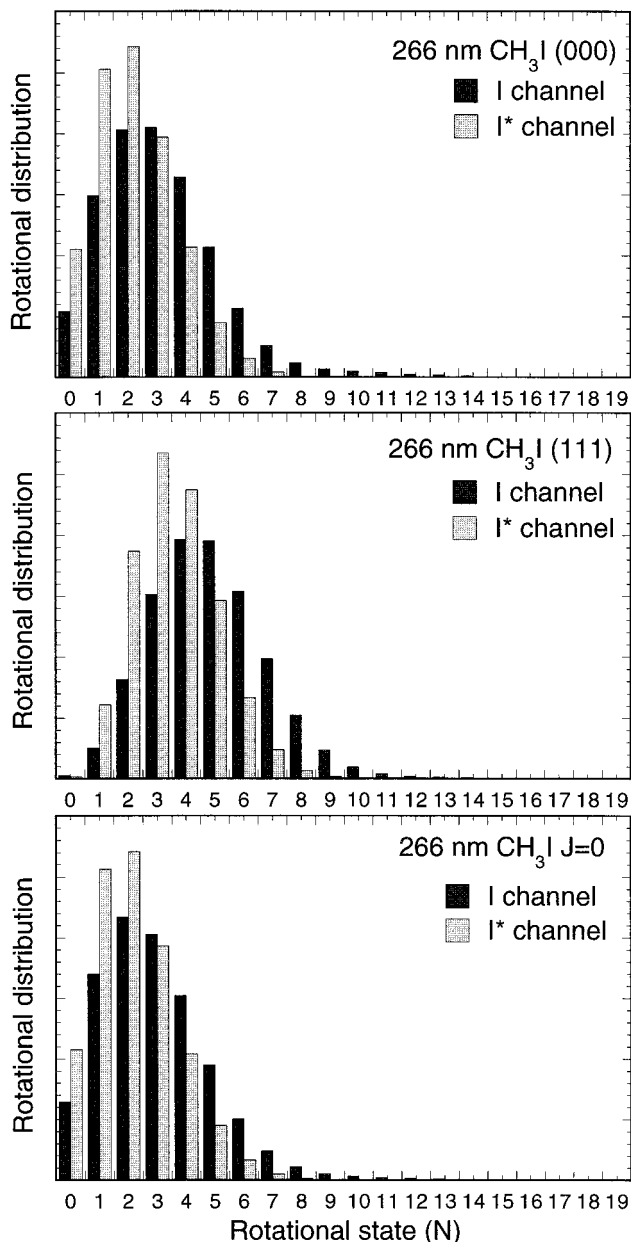


**Figure 8.** Calculated vibrational state averaged rotational distributions of  $\text{CH}_3$  from the  $|000\rangle$  (upper panel) and  $|111\rangle$  (middle panel) states. The lower panel is for the hypothetical  $J = 0$  dissociation. Both the parallel and perpendicular transitions are included.

distribution in the  $\text{I}^*$  channel has a peak at  $N = 4$  ( $K = 1$ ), which agrees reasonably well with the calculated  $\text{I}^*$  channel  $\text{CD}_3$  distribution (lower panel in Figure 9) which has a peak at  $N = 5$ . The rotational distribution obtained by Kim et al.<sup>23</sup> appears to be much colder. With no initial parent rotational state selection, the peak was found experimentally at  $N = 3$  ( $K = 0$ ) for cold parent molecules,<sup>21,22</sup> consistent with our distribution in upper panel in Figure 9. The extension of the distribution to  $N = 11$  for the  $\text{I}^*$  channel and to  $N = 19$  for the  $\text{I}$  channel is also consistent with the observation of Powis and Black.<sup>19</sup>

**D.  $\text{I}^*$  Quantum Yield.** The  $\text{I}^*$  quantum yield is an important indicator of nonadiabatic transitions between the  ${}^3\text{Q}_{0+}$  and  ${}^1\text{Q}_1$  states during the dissociation. Figure 10 presents the  $\text{I}^*$  yield for the dissociation of both  $\text{CH}_3\text{I}$  and  $\text{CD}_3\text{I}$  as a function of photon energy. In both cases, the  $\text{I}^*$  yield is a slowly varying function of the energy near the absorption maximum. The  $\text{I}^*$  yield is sensitive to the excitation mode and the overall rotation of the parent molecule. As expected, the calculated  $\text{I}^*$  yield is



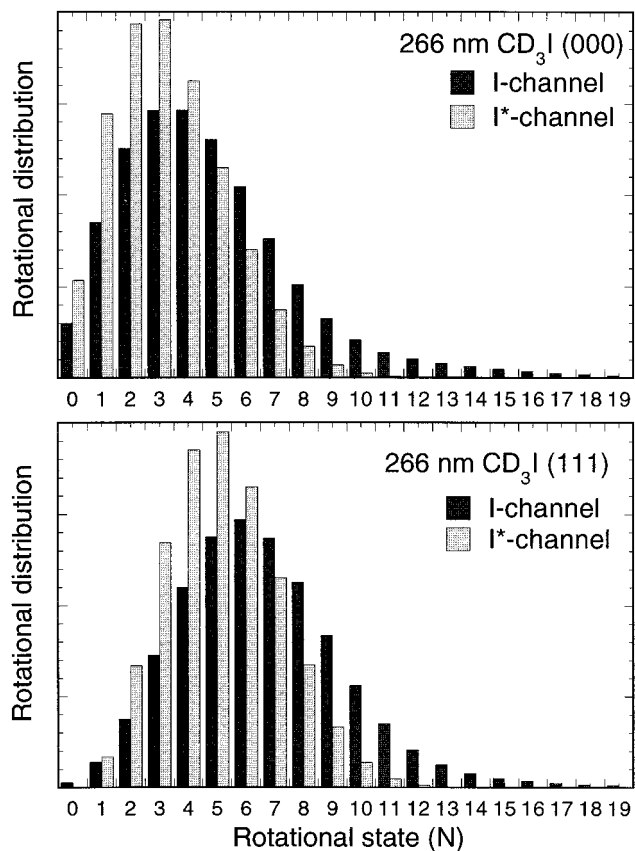


**Figure 9.** Calculated vibrational state averaged rotational distributions of CD<sub>3</sub> from the |000> (upper panel) and |111> (lower panel) states. Both the parallel and perpendicular transitions are included.

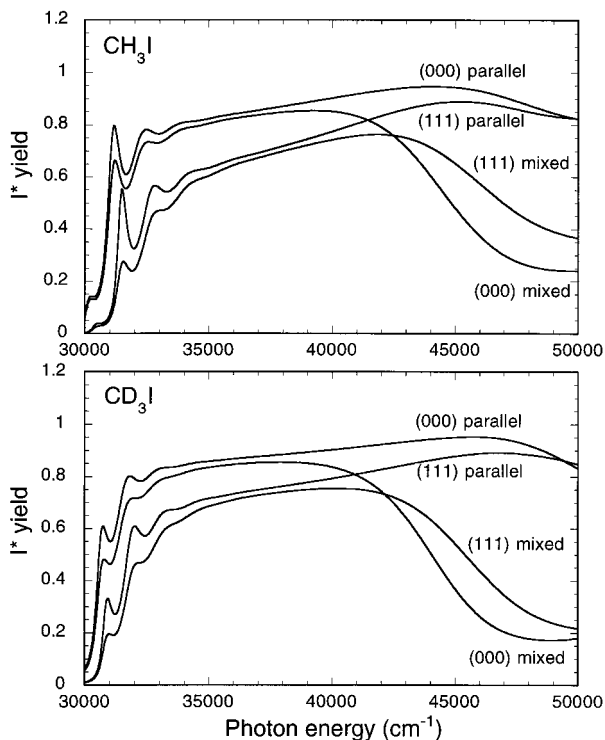


**Figure 10.** Calculated photon energy dependence of I\* quantum yield for both CH<sub>3</sub>I and CD<sub>3</sub>I from different initial excitations.

larger if the excitation involves only the parallel transition. At 266 nm, the I\* yields for mixed parallel/perpendicular and pure parallel excitation from the  $|J_i M_i K_i\rangle = |000\rangle$  state are 0.84 and 0.86 for CH<sub>3</sub>I, and 0.85 and 0.88 for CD<sub>3</sub>I. At 248 nm, the

corresponding values are 0.85 and 0.91 for CH<sub>3</sub>I, and 0.83 and 0.90 for CD<sub>3</sub>I. These values are not very different from previous calculations.<sup>4,39,40,44</sup> It is also noted that the isotope effect in the I\* yield is not particularly conspicuous, as observed in previous theoretical calculations.<sup>4,40</sup>

The perpendicular excitation to the <sup>1</sup>Q<sub>1</sub> state affects the I\* yield mostly at high energies. As shown in Figure 10, the I\* yield above 40000 cm<sup>-1</sup> is dramatically lower than the pure parallel case if both excited states are populated in the initial excitation. The calculated I\* yield appears to have strong dependence on the parent rotation. Excitation from the  $|J_i M_i K_i\rangle = |111\rangle$  state shows a marked decrease in the I\* yield, even with pure parallel excitation. Apparently, the excitation in *K* significantly enhances transitions from the <sup>3</sup>Q<sub>0+</sub> state to the <sup>1</sup>Q<sub>1</sub> state. This can be readily understood from the fact that the coupling between the two diabatic states is proportional to sin  $\chi$ . Since the coupling is strictly zero at the C<sub>3v</sub> geometry ( $\chi = 0$ ), transitions between the two diabates require distortion from the C<sub>3v</sub> geometry.<sup>41,46</sup> The angular wave function for *K* > 0 is zero at  $\chi = 0$  and has significantly more amplitude away from linearity than its *K* = 0 counterpart. Consequently, stronger transitions ensue.

Experimental values of the I\* yield vary in a wide range (see Table 3 in ref 3). Using an ionization imaging technique, Eppink and Parker<sup>3</sup> recently observed a weak frequency dependence of the I\* yield in the range from 280 to 240 nm. At 266 nm, the I\* yield was found to be 0.73 and changes little in the vicinity. Our results from the |000> parent state are somewhat higher than the experimental observation. The I\* yield at 266 nm from the rotationally excited |111> state is significantly smaller (0.71).

For the parent state of |000> of CH<sub>3</sub>I, the calculated I\* yields at 266 nm for the CH<sub>3</sub> vibrational states  $\nu = 0, 1, 2$  are found to be 0.94, 0.75, 0.55, in excellent agreement with the recent experiments of Eppink and Parker<sup>3</sup> (0.94, 0.83, 0.51) and of Loo et al.<sup>13</sup> (0.92, 0.77, 0.47). The corresponding I\* yield for the parent state of |111> was calculated to be 0.90, 0.62, and 0.51 at 266 nm. The decreasing I\* yield with the methyl umbrella vibrational quantum number reflects the fact that the methyl fragment in the I channel is much more vibrationally excited than that in the I\* channel. The corresponding values for  $\nu = 0, 1, 2, 3$  of CD<sub>3</sub> from the dissociation of the |000> state of CD<sub>3</sub>I at 266 nm (0.99, 0.93, 0.51, 0.08) reproduce the trend observed experimentally by Chandler et al.<sup>21</sup> (0.96, 0.92, 0.79, 0.42) and by Loo et al.<sup>18</sup> (0.95, 0.92, 0.84, 0.60). The quantitative discrepancies between theory and experiment could arise from uncertainties in highly excited CD<sub>3</sub> vibrational state populations.

**E. State-Resolved Angular Distribution of the CD<sub>3</sub> Fragment.** Bernstein et al.<sup>26</sup> have demonstrated previously that the fragment angular distribution upon the photodissociation of the hexapole oriented methyl iodide is asymmetric about the polarization direction of the photolysis laser. Combined with a product imaging technique, Janssen et al.<sup>25</sup> have measured internal state resolved product angular distributions for oriented CD<sub>3</sub>I. These authors showed that in the strong field limit the CD<sub>3</sub> product recoils with angles near the SF *z'* axis when the parent molecule is prepared in the  $|J_i M_i K_i\rangle = |111\rangle$  state. We have calculated the angular distribution for a number of fragment states using eq 9.

The upper panel in Figure 11 shows the angular distribution for the  $\nu = 0, N = 1$  state of CD<sub>3</sub> in the I\* channel from the dissociation of the *J<sub>i</sub>, K<sub>i</sub> = 1, 1* parent states with three different *M<sub>i</sub>*. The angular distribution for the *M<sub>i</sub> = 1* state maximizes

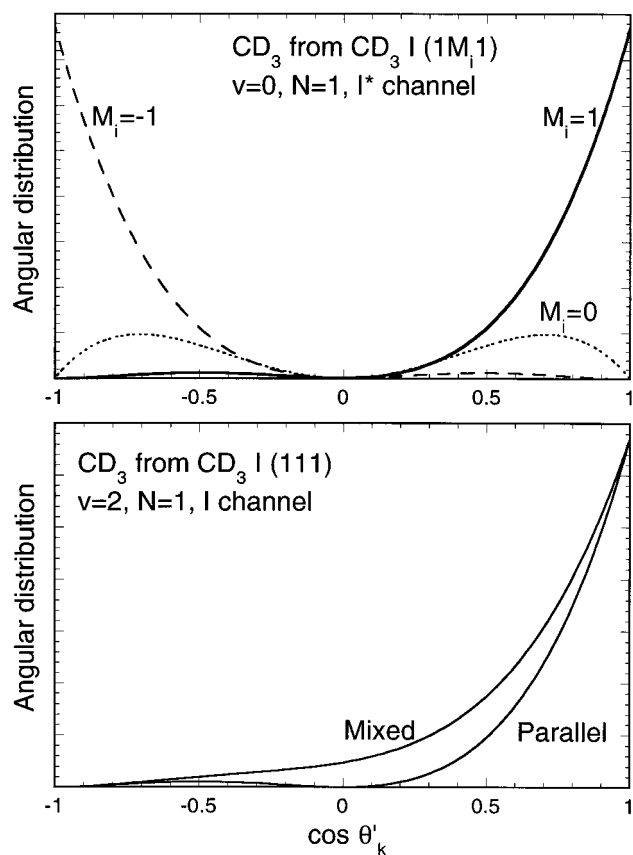


**Figure 11.** Angular distributions of the  $\nu = 0$ ,  $N = 1$  state of  $\text{CD}_3$  in the  $I^*$  channel (upper panel) and  $\nu = 2$ ,  $N = 1$  state in the  $I$  channel (lower panel) from the photodissociation of initially oriented  $\text{CD}_3\text{I}$  ( $J_i, K_i = 1, 1$ ). The scattering angle is measured from the SF  $z'$  axis.

near  $\theta'_k = 0^\circ$  and decreases with increasing angle, owing to the predominantly parallel excitation. It is in excellent agreement with the experimental observation, which is not surprising since the angular distribution is primarily determined by the orientation of the parent molecule in such fast and axial dissociation. The distribution for  $M_i = -1$  is a mirror image of that for  $M_i = 1$ , while the  $M_i = 0$  distribution is symmetric about  $90^\circ$ . If all three distributions are added together, the overall distribution corresponds to the limit of randomly oriented parent molecules, which can be described by  $\cos^2\theta'_k$  with the anisotropy parameter  $\beta = 2$ .<sup>50</sup> For this internal state, the contribution from the perpendicular excitation to the  $^1Q_1$  state is minimal.

We have also calculated angular distributions for other internal states where the perpendicular excitation does play an important role. The lower panel in Figure 11 displays such a distribution for the  $\nu = 3$ ,  $N = 1$  state of  $\text{CD}_3$  in the  $I$  channel, produced from the parent state  $|J_i M_i K_i\rangle = |111\rangle$ . While the distribution resulted from pure parallel excitation to the  $^3Q_0+$  state is essentially the same as the  $M_i = 1$  case in the upper panel, the distribution from mixed parallel/perpendicular excitation produces a significant increase of population near  $90^\circ$ , due to the contribution from the  $^1Q_1$  state.

#### IV. Conclusion

In this work, we revisited the photodissociation of methyl iodide in its  $\tilde{A}$  band, using new and improved PESs. Our three-dimensional model contains the essential degrees of freedom in the dissociation dynamics and allows transitions between the  $^3Q_0+$  and  $^1Q_1$  electronic states. More importantly, the overall rotation of the dissociating system is included. The quantum

dynamics was studied using the Chebyshev polynomial propagation. The calculated absorption spectrum shows much improvement in both the center position and width over that obtained from the previous PESs. The improvement can be attributed to the higher quality of the new PESs in the Franck-Condon region, which were obtained using a large basis and more configurations. A better agreement with experimental data in the internal state distributions of the photofragments has also been achieved. Our results indicate that the overall rotation has significant effects on vibrational and particularly rotational distributions of the methyl fragment. An interesting finding in this system is that the excitation in  $K$  can significantly enhance transitions between the diabatates. This is because the initial angular wave function has larger amplitudes away from the  $C_{3v}$  geometry where the potential coupling is zero. We have also calculated product state resolved angular distributions for the dissociation of oriented parent molecules. Our results are in excellent agreement with experimental measurement.

A major remaining uncertainty for this system is the relative strength of the transition dipole moments to the two excited states. The latest experiment based on product velocity imaging concluded that the contribution of the  $^1Q_1$  state is minimal throughout the  $\tilde{A}$  band, whereas the ab initio theory indicates a significant  $^1Q_1$  component in the high-energy wing of the absorption spectrum. Another issue is the strength of the nonadiabatic coupling. The theoretical  $I^*$  yield near the center of the absorption band from the  $|000\rangle$  parent state is significant higher than experiment values. Finally, it is clear that our model provides no information on the rotational distribution of the methyl fragment along its figure axis or the C-H stretch excitation. These questions have to be addressed with higher dimensional models.

**Acknowledgment.** This work at UNM was supported by the National Science Foundation (CHE-9713995). One of us (D.X.) was supported in part by National Natural Science Foundation of China. The ab initio calculations were partly performed at the Computer Center of the Institute for Molecular Science. Y.A. thanks a Grant-in-Aid for Scientific Research from the Ministry of Education, Science, Sport and Culture of Japan. R.K. is grateful to the United States Israel Binational Science Foundation for support. We also thank Prof. David Nesbitt for remeasuring the absorption spectrum of  $\text{CH}_3\text{I}$ .

#### References and Notes

- (1) Mulliken, R. S. *J. Chem. Phys.* **1940**, *8*, 382.
- (2) Gedanken, A.; Rowe, M. D. *Chem. Phys. Lett.* **1975**, *34*, 39.
- (3) Eppink, A. T. J. B.; Parker, D. H. *J. Chem. Phys.* **1998**, *109*, 4758.
- (4) Guo, H. *J. Chem. Phys.* **1992**, *96*, 6629.
- (5) Johnson, B. R.; Kittrell, C.; Kelly, P. B.; Kinsey, J. L. *J. Phys. Chem.* **1996**, *100*, 7743.
- (6) Eppink, A. T. J. B.; Parker, D. H. *J. Chem. Phys.* **1999**, *110*, 832.
- (7) Knee, J. L.; Khundkar, L. R.; Zewail, A. H. *J. Chem. Phys.* **1985**, *83*, 2461.
- (8) Imre, D.; Kinsey, J. L.; Sinha, A.; Krenos, J. *J. Phys. Chem.* **1984**, *88*, 3956.
- (9) Hale, M. O.; Galica, G. E.; Glogover, S. G.; Kinsey, J. L. *J. Phys. Chem.* **1986**, *90*, 4997.
- (10) Galica, G. E.; Johnson, B. R.; Kinsey, J. L.; Hale, M. O. *J. Phys. Chem.* **1991**, *95*, 7994.
- (11) Lao, K. Q.; Person, M. D.; Xayariboun, P.; Butler, L. J. *J. Chem. Phys.* **1990**, *92*, 823.
- (12) Strobel, A.; Fischer, I.; Lochschmidt, A.; Muller-Dethlefs, K.; Bondybey, V. E. *J. Phys. Chem.* **1994**, *98*, 2024.
- (13) Loo, R. O.; Haerri, H.-P.; Hall, G. E.; Houston, P. L. *J. Chem. Phys.* **1989**, *90*, 4222.
- (14) Hall, G. E.; Sears, T. J.; Frye, J. M. *J. Chem. Phys.* **1989**, *90*, 6234.
- (15) Suzuki, T.; Kanamori, H.; Hirota, E. *J. Chem. Phys.* **1991**, *94*, 6607.
- (16) Zhu, Q.; Continetti, R. E.; Zhao, X.; Balko, B.; Hints, E.; Lee, Y. T., private communication.

- (17) Zahedi, M.; Harrison, J. A.; Nibler, J. W. *J. Chem. Phys.* **1994**, *100*, 4043.
- (18) Loo, R. O.; Hall, G. E.; Haerri, H.-P.; Houston, P. L. *J. Phys. Chem.* **1988**, *92*, 5.
- (19) Powis, I.; Black, J. F. *J. Phys. Chem.* **1989**, *93*, 2461.
- (20) Chandler, D. W.; Thoman, J. W.; Janssen, M. H. M.; Parker, D. H. *Chem. Phys. Lett.* **1989**, *156*, 151.
- (21) Chandler, D. W.; Janssen, M. H. M.; Stolte, S.; Strickland, R. N.; Thoman, J. W.; Parker, D. H. *J. Phys. Chem.* **1990**, *94*, 4839.
- (22) Janssen, M. H. M.; Parker, D. H.; Sitz, G. O.; Stolte, S.; Chandler, D. W. *J. Phys. Chem.* **1991**, *95*, 8007.
- (23) Kim, D. Y.; Brandstater, N.; Pipes, L.; Garner, T.; Baugh, D. *J. Phys. Chem.* **1995**, *99*, 4364.
- (24) Mastenbroek, J. W. G.; Taatjes, C. A.; Nauta, K.; Janssen, M. H. M.; Stolte, S. *J. Phys. Chem.* **1995**, *99*, 4360.
- (25) Janssen, M. H. M.; Mastenbroek, J. W. G.; Stolte, S. *J. Phys. Chem. A* **1997**, *101*, 7605.
- (26) Gandhi, S. R.; Curtiss, T. J.; Bernstein, R. B. *Phys. Rev. Lett.* **1987**, *59*, 2951.
- (27) Parker, D. H.; Bernstein, R. B. *Annu. Rev. Phys. Chem.* **1989**, *40*, 561.
- (28) Seideman, T. *J. Chem. Phys.* **1995**, *102*, 6487.
- (29) Torres, E. A.; Kim, D. Y.; Pipes, L. C.; Baugh, D. A.; Seideman, T. *J. Chem. Soc., Faraday Trans.* **1997**, *93*, 931.
- (30) Shapiro, M.; Bersohn, R. *J. Chem. Phys.* **1980**, *73*, 3810.
- (31) Shapiro, M. *J. Phys. Chem.* **1986**, *90*, 3644.
- (32) Guo, H.; Schatz, G. C. *J. Chem. Phys.* **1990**, *93*, 393.
- (33) Guo, H.; Lao, K. Q.; Schatz, G. C.; Hammerich, A. D. *J. Chem. Phys.* **1991**, *94*, 6562.
- (34) Sundberg, R. L.; Imre, D.; Hale, M. O.; Kinsey, J. L.; Coalson, R. D. *J. Phys. Chem.* **1986**, *90*, 5001.
- (35) Guo, H.; Schatz, G. C. *J. Phys. Chem.* **1991**, *95*, 3091.
- (36) Wedlock, M. R.; Jensen, E.; Butler, L. J.; Freed, K. *J. Phys. Chem.* **1991**, *95*, 8096.
- (37) Tadjeddine, M.; Flament, J. P.; Teichteil, C. *Chem. Phys.* **1987**, *118*, 45.
- (38) Yabushita, S.; Morokuma, K. *Chem. Phys. Lett.* **1988**, *153*, 517.
- (39) Amatatsu, Y.; Morokuma, K.; Yabushita, S. *J. Chem. Phys.* **1991**, *94*, 4858.
- (40) Amatatsu, Y.; Yabushita, S.; Morokuma, K. *J. Chem. Phys.* **1996**, *104*, 9783.
- (41) Guo, H. *J. Chem. Phys.* **1992**, *96*, 2731.
- (42) Guo, H. *Chem. Phys. Lett.* **1991**, *187*, 360.
- (43) Manthe, U.; Hammerich, A. D. *Chem. Phys. Lett.* **1993**, *211*, 7.
- (44) Hammerich, A. D.; Manthe, U.; Kosloff, R.; Meyer, H.-D.; Cederbaum, L. S. *J. Chem. Phys.* **1994**, *101*, 5623.
- (45) Huang, Z.-H.; Guo, H. *J. Chem. Phys.* **1993**, *98*, 3395.
- (46) Person, M. D.; Kash, P. W.; Butler, L. J. *J. Chem. Phys.* **1991**, *94*, 2557.
- (47) Schatz, G. C.; Kuppermann, A. *J. Chem. Phys.* **1976**, *65*, 4642.
- (48) *Software Library of the Computer Center for Institute for Molecular Science.*
- (49) Schmidt, M. W.; Baldrige, K. K.; Boatz, J. A.; Elbert, S. T.; Gordon, M. S.; Jensen, J. H.; Koseki, S.; Matsunaga, N.; Nguyen, K. A.; Su, S. J.; Windus, T. L.; Dupui, M.; Montgomery, J. A. *J. Comput. Chem.* **1993**, *14*, 1347.
- (50) Balint-Kurti, G. G.; Shapiro, M. *Chem. Phys.* **1981**, *61*, 137.
- (51) Balint-Kurti, G. G.; Shapiro, M. Quantum theory of molecular photodissociation. In *Photodissociation and Photoionization*; Lawley, K. P., Ed.; Wiley: New York, 1985; p 403.
- (52) Schinke, R. *Photodissociation Dynamics*; Cambridge University Press: Cambridge, 1993.
- (53) Chen, R.; Guo, H. *Comput. Phys. Comm.* **1999**, *119*, 19.
- (54) Tal-Ezer, H.; Kosloff, R. *J. Chem. Phys.* **1984**, *81*, 3967.
- (55) Guo, H. *J. Chem. Phys.* **1998**, *108*, 2466.
- (56) Guo, H.; Seideman, T. *Phys. Chem. Chem. Phys.* **1999**, *1*, 1265.
- (57) Chen, R.; Guo, H. *J. Chem. Phys.* **1996**, *105*, 3569.
- (58) Lanczos, C. *J. Res. Natl. Bur. Stand.* **1950**, *45*, 255.
- (59) King, W. T.; Mills, I. M.; Crawford, B. *J. Chem. Phys.* **1957**, *27*, 455.
- (60) Herzberg, G. *Molecular Spectra and Molecular Structure, Vol. 3, Electronic Spectra of Polyatomic Molecules*; Van Nostrand: Princeton, 1966.
- (61) Colbert, D. T.; Miller, W. H. *J. Chem. Phys.* **1992**, *96*, 1982.
- (62) Light, J. C.; Hamilton, I. P.; Lill, J. V. *J. Chem. Phys.* **1985**, *82*, 1400.
- (63) Corey, G. C.; Lemoine, D. *J. Chem. Phys.* **1992**, *97*, 4115.
- (64) Echave, J.; Clary, D. C. *Chem. Phys. Lett.* **1992**, *190*, 225.
- (65) Kosloff, D.; Kosloff, R. *J. Comput. Phys.* **1983**, *52*, 35.
- (66) Amatashu, Y.; Yabushita, S.; Morokuma, K. *J. Chem. Phys.* **1994**, *100*, 4894.